

Adaptive integration of history variables in constrained mixture models for organ-scale growth and remodeling

Amadeus M. Gebauer^{1*}, Martin R. Pfaller², Jason M. Szafron³,
Wolfgang A. Wall^{1,4}

¹Institute for Computational Mechanics, Technical University of Munich, Boltzmannstr. 15, Garching, 85748, Germany.

²Pediatric Cardiology, Stanford Maternal & Child Health Research Institute, and Institute for Computational and Mathematical Engineering, Stanford University, Stanford, USA.

³Department of Biomedical Engineering, Carnegie Mellon University, Pittsburgh, USA.

⁴Munich Institute of Biomedical Engineering, Technical University of Munich, Boltzmannstr. 11, Garching, 85748, Germany.

*Corresponding author(s). E-mail(s): amadeus.gebauer@tum.de;
Contributing authors: pfaller@stanford.edu; jszafron@andrew.cmu.edu;
wolfgang.a.wall@tum.de;

Abstract

In the last decades, many computational models have been developed to predict soft tissue growth and remodeling (G&R). The constrained mixture theory describes fundamental mechanobiological processes in soft tissue G&R and has been widely adopted in cardiovascular models of G&R. However, even after two decades of work, large organ-scale models are rare, mainly due to high computational costs (model evaluation and memory consumption), especially in long-range simulations. We propose two strategies to adaptively integrate history variables in constrained mixture models to enable large organ-scale simulations of G&R. Both strategies exploit that the influence of deposited tissue on the current mixture decreases over time through degradation. One strategy is independent of external loading, allowing the estimation of the computational resources ahead of the simulation. The other adapts the history snapshots based on the local mechanobiological environment so that the additional integration errors can be controlled and kept negligibly small, even in G&R scenarios with severe perturbations. We analyze the adaptively integrated constrained mixture model on a tissue patch for a parameter study and show the performance under different G&R scenarios. To confirm that adaptive strategies enable large organ-scale examples, we show simulations of different hypertension conditions with a real-world example of a biventricular heart discretized with a finite element mesh. In our example, adaptive integrations sped up simulations by a factor of three and reduced memory requirements to one-sixth. The reduction of the computational costs gets even more pronounced for simulations over longer periods. Adaptive integration of the history variables allows studying more finely resolved models and longer G&R periods while computational costs are drastically reduced and largely constant in time.

Keywords: Growth and remodeling, Constrained mixture model, Computational modeling, Mechanobiology, Organ-scale

1 Introduction

Living biological tissue on the microstructural scale consists of multiple constituents (e.g., collagen fibers, elastin fibers, different kinds of cells, and more) with relevant effects on the macroscopic or organ scale. Additionally, biological tissue can grow (change mass) and remodel (change microstructure) continuously in response to mechanical and chemical cues with the ultimate goal of retaining a local preferred mechanobiological environment, a so-called homeostatic state, or, better, to allow for allostasis, an even more crucial process for living systems.

A key process involved in this mechanobiological activity is turnover, i.e., the continuous deposition of new and degradation of existing mass [7]. During tissue maintenance, turnover is balanced such that there is no effective change in mass or microstructure. Unbalanced turnover can result in excessive mass deposition, e.g., fibrosis after injury or disease.

Various computational models have been developed on different scales and complexity levels to increase understanding of soft tissue growth and remodeling (G&R). A family of methods that model these key mechanobiological aspects (i.e., homeostasis and turnover) builds upon the constrained mixture theory [8, 17, 20].

The constrained mixture model [17] assumes tissue to consist of multiple constituents. Mass increments of the constituents are added at every point in time into the mixture to model the key mechanobiological process of production. Once deposited, the mass increments are actively degraded over time. Models based upon the constrained mixture theory are widespread in vascular G&R [16] and were recently adopted to cardiac G&R [11].

Organ-scale constrained mixture models typically use the finite element method for spatial discretization. Early models of thin-walled vascular geometries use 2D membrane elements (e.g., [2, 30, 35]) and, later, also models with 3D elements have been developed [14, 23, 33]. However, large organ-scale models are still missing, mainly due to the high computational costs.

In constrained mixture models, one needs to track the deformation state of every mass increment deposited at every prior point in time, resulting in typically high computational costs. Hence,

different variants of the constrained mixture theory have been developed to reduce computational costs and allow larger organ-scale simulations.

There are so-called homogenized constrained mixture models [8] that apply a temporal homogenization of deposition and degradation of constituents. In these models, the integration of the history variables reduces to ordinary differential equations. These models have been applied to organ-scale models of vascular G&R on 3D thick-walled cylinders [5, 6] and patient-specific geometries [25], and, recently, for cardiac G&R [11]. The homogenization can fail in situations with rapid changes in load and mass production, resulting in appreciable differences between homogenized and classical constrained mixture models (see, for example, Section 3.2 and Figure 5 in Cyron et al. [8]). Additionally, losing track of the individual mass increments precludes modeling increased degradation of individual fibers caused by excessive tension and damage as proposed by Baek et al. [3].

Another approach is to compute only the mechanobiological steady-state at the end of active G&R. This approach, called equilibrated constrained mixture model [20, 22], is particularly useful if changes in the external loads are slow compared to the involved turnover time constants. The equilibration can, however, not predict G&R that does not reach a new mechanobiological equilibrium, e.g., in cases where mechanobiological sensing is disrupted. In this paper, we will analyze a mechanobiologically unstable G&R example that cannot be described by the equilibrated constrained mixture model.

Challenging G&R scenarios, where both computationally cheaper variants fail, require to solve the classical constrained mixture model. In this work, we focus on the classical constrained mixture approach, where a large integral over the deposition and degradation history is solved. These integrals are typically solved with a trapezoidal rule [23, 33, 35] or Simpson's rule [14] with *equal-sized* timesteps. To bound computational costs, a few models assume a maximum survival time of deposited mass, after which contributions to the current mixture response are neglected [14, 23, 35]. This can lead to sudden jumps in behavior if the deformation since deposition is large and the constituents have a non-linear material behavior. Here, we propose to adaptively

integrate history variables in constrained mixture models by exploiting that the influence of deposited mass decreases over time through active degradation. Adaptive history integration reduces the computational costs tremendously and still avoids the definition of a maximum survival time while keeping the additional integration error negligibly small. In our organ-scale example, we focus on cardiac G&R, but the methods are applicable to any constrained mixture model.

In Section 2, we briefly summarize the equations for constrained mixture models in the context of finite element methods and describe two strategies to adaptively integrate the G&R history. Section 3 compares the adaptive integration approaches with the non-adaptive case on a simple tissue patch example. To demonstrate that the adaptive integration enables constrained mixture models for large 3D organ-scale examples, we apply the constrained mixture model to a patient-specific geometry of two ventricles in Section 4. Finally, we discuss and summarize the findings.

2 Mathematical modeling

To describe G&R on the organ scale, we use nonlinear continuum mechanics [13]. The material point \mathbf{X} in the reference configuration \mathcal{B}_0 is mapped to its spatial point \mathbf{x} in the current configuration \mathcal{B}_s at G&R time s ¹ via

$$\mathbf{x} : \mathcal{B}_0 \times [0, \infty) \rightarrow \mathcal{B}_s, \quad (\mathbf{X}, s) \mapsto \mathbf{x}(\mathbf{X}, s).$$

Without loss of generality, we assume that the configuration at $s = 0$ is the reference configuration. The displacement of point \mathbf{X} is $\mathbf{u} = \mathbf{x} - \mathbf{X}$. The deformation gradient is $\mathbf{F} = \frac{\partial \mathbf{x}}{\partial \mathbf{X}}$ with determinant $J = \det \mathbf{F}$.

The tissue consists of multiple structurally significant constituents, which are modeled individually. These constituents are locally entangled and deform together, i.e., the displacement field of each constituent is the same as the displacement field of the mixture ($\mathbf{u} = \mathbf{u}^i$). We denote quantities related to a specific constituent with superscript i .

¹We use s for the G&R time to emphasize that G&R takes place on the large timescale that is different from the typical timescale of a heartbeat usually denoted with t .

The stress response is homogenized across the constituents, i.e.,

$$\mathbf{S} = 2 \frac{\partial \Psi}{\partial \mathbf{C}} = \sum_i \rho_0^i 2 \frac{\partial W^i}{\partial \mathbf{C}} = \sum_i \rho_0^i \tilde{\mathbf{S}}^i, \quad (1)$$

where \mathbf{S} is second Piola-Kirchhoff stress of the mixture, $\mathbf{C} = \mathbf{F}^T \mathbf{F}$ is the right Cauchy-Green deformation tensor, Ψ is the Helmholtz free-energy function of the mixture, and for each constituent i , ρ_0^i is the reference mass density per mixture volume, W^i is the strain energy per unit mass and $\tilde{\mathbf{S}}^i$ is the fictitious, specific second Piola-Kirchhoff stress tensor. We denote it *fictitious* and *specific* since it is the stress tensor of the constituent only in case the mass fraction is one and after multiplication with the mass density. This homogenization across the constituents of the stress response is called a simple *rule-of-mixture* [17] and has the benefit that only the equilibrium for the mixture has to be solved and not for each constituent individually. The mechanical equilibrium written in the form of the principle of virtual work [13] is

$$\delta W = \frac{1}{2} \int_{\mathcal{B}_0} \mathbf{S} : \delta \mathbf{C} \, dV = 0. \quad (2)$$

We neglect inertial effects since G&R is typically happening in the time scale of weeks and months.

2.1 Mass production and removal

We solve our equilibrium equations using a total Lagrangian approach. The production and degradation of mass must, therefore, also be represented in the reference configuration. We describe the mass change by an evolution of the reference mass density per mixture volume $\rho_0^i = \rho_0^i(s)$ [5].

The evolution of mass is driven by continuous deposition and degradation of tissue. To model deposition and degradation individually, we split the net mass production rate $\dot{\rho}_0^i$ into a true mass production rate $\dot{\rho}_{0+}^i \geq 0$ and true mass degradation rate $\dot{\rho}_{0-}^i \leq 0$, i.e.,

$$\dot{\rho}_0^i = \dot{\rho}_{0+}^i + \dot{\rho}_{0-}^i. \quad (3)$$

Both evolutions can be chosen individually with the constraint that deposition and degradation must compensate during homeostasis, i.e., $\dot{\rho}_0^i = 0$

for pure maintenance. To remove the dimensionality of equation (3), we scale the quantity by the initial reference mass density $\rho_0^i(s=0)$ and obtain the non-dimensional growth scalar κ^i with

$$\kappa^i(s) = \frac{\rho_0^i(s)}{\rho_0^i(s=0)},$$

which is one if the mass does not change, larger than one during growth, and smaller than one during atrophy. Equation (3) can then be written as

$$\dot{\kappa}^i(s) = \dot{\kappa}_+^i + \dot{\kappa}_-^i, \quad \text{with} \quad \dot{\kappa}_\pm^i = \frac{\dot{\rho}_{0\pm}^i}{\rho_0^i(s=0)}.$$

The kinetics of cell apoptosis and, generally, tissue degradation is complex and can depend on the current mechanobiological environment (see, for example, [32]). For simplicity, we will assume a simple Poisson degradation process similar to radioactive decay. The dimensionless mass removal rate is, therefore,

$$\dot{\kappa}_-^i = -\frac{\kappa^i}{T^i}, \quad (4)$$

where T^i is the mean survival time of the constituent.

The survival function $q^{i(\tau)}$ is the fraction of the mass deposited at time τ that is still surviving at time s . For a simple Poisson degradation, it is

$$q^{i(\tau)}(s) = \exp\left(-\frac{s-\tau}{T^i}\right).$$

To link new production of tissue to the mechanobiological state of the tissue, we follow Braeu et al. [5] and assume that the true mass production rate is

$$\dot{\kappa}_+^i = \kappa^i \left[\frac{1}{T^i} + \mathbf{K}_\sigma^i : (\boldsymbol{\sigma}_R^i - \boldsymbol{\sigma}_h^i) \right], \quad (5)$$

where \mathbf{K}_σ^i is a gain-type second-order tensor. The first term in brackets ensures that the basal mass production rate compensates for the continuous degradation of mass with time constant T^i during homeostasis (equation (4)). The second term is unequal to zero if the Cauchy stress differs from the homeostatic stress, and hence, net mass will be produced or degraded for compensation. The

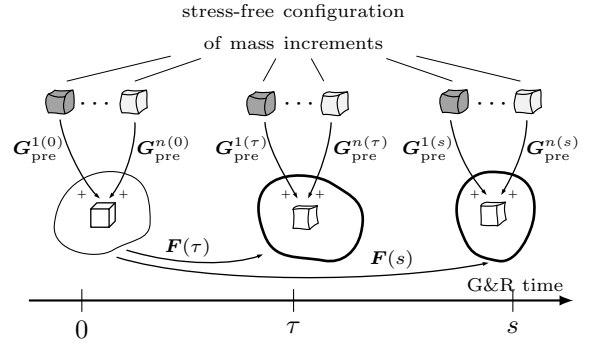


Fig. 1 Configurations during G&R. At every point in time, new mass increments of each constituent are added to the mixture with a prestretch $\mathbf{G}_{\text{pre}}^{i(\tau)}$.

tensor $\boldsymbol{\sigma}_R^i$ is the co-rotated Cauchy stress of the constituent [5] and $\boldsymbol{\sigma}_h^i$ is its homeostatic setpoint.

Biological tissue often consists of fibrous constituents like muscle cells and collagen fibers. These constituents are often modeled as quasi-one-dimensional fiber families. For such constituents, only the components in the direction of the fiber are unequal to zero [5], such that equation (5) reduces to

$$\dot{\kappa}_+^i = \kappa^i \left[\frac{1}{T^i} + k_\sigma^i \frac{\sigma^i - \sigma_h^i}{\sigma_h^i} \right], \quad (6)$$

with $k_\sigma^i = \boldsymbol{\sigma}_h^i \mathbf{K}_\sigma^i : (\mathbf{f}_0^i \otimes \mathbf{f}_0^i)$, $\sigma^i = \boldsymbol{\sigma}_R^i : (\mathbf{f}_0^i \otimes \mathbf{f}_0^i)$, $\sigma_h^i = \boldsymbol{\sigma}_h^i : (\mathbf{f}_0^i \otimes \mathbf{f}_0^i)$, and \mathbf{f}_0^i is the unit vector pointing in the direction of the fiber in the reference configuration.

2.2 Turnover

The constrained mixture theory [17] models turnover by continuously adding mass increments into the mixture that will then degrade over time.

In every infinitesimal time interval ds , a new mass increment with mass $\dot{\rho}_{0+}^i ds$ and prestretch $\mathbf{G}_{\text{pre}}^i$ is added to the mixture as shown in Figure 1. Once deposited, the mass increment is continuously degraded over time following the survival function $q^{i(\tau)}$. Hence, the reference mass density

evolves with

$$\rho_0^i(s) = q^{i(0)}(s)\rho_0^i(s=0) + \int_0^s q^{i(\tau)}(s)\hat{\rho}_{0+}^i(\tau)d\tau.$$

The first term outside of the integral describes the tissue that is initially present at $s = 0$. This equation can also be rewritten in terms of the nondimensional growth scalar, i.e.,

$$\kappa^i(s) = q^{i(0)}(s) + \int_0^s q^{i(\tau)}(s)\hat{\kappa}_+^i(\tau)d\tau. \quad (7)$$

Following the *rule-of-mixture* approach of equation (1) on the constituent level, the fictitious second Piola-Kirchhoff stress response of the constituent i is

$$\tilde{\mathbf{S}}^i(s) = \frac{1}{\kappa^i(s)} \left[q^{i(0)}(s)\tilde{\mathbf{S}}^{i(0)}(\mathbf{F}_e^{i(0)}) + \dots \int_0^s q^{i(\tau)}(s)\hat{\kappa}_+^i(\tau)\tilde{\mathbf{S}}^{i(\tau)}(\mathbf{F}_e^{i(\tau)})d\tau \right]. \quad (8)$$

where $\tilde{\mathbf{S}}^{i(\tau)}$ is the fictitious, specific second Piola-Kirchhoff stress of the mass increment added at the intermediate time τ and $\mathbf{F}_e^{i(\tau)}$ is its total elastic deformation. The total elastic deformation gradient for the initially present mass is

$$\mathbf{F}_e^{i(0)} = \mathbf{F}(s)\mathbf{G}_{\text{pre}}^{i(0)},$$

and for the later deposited mass, it is

$$\mathbf{F}_e^{i(\tau)} = \mathbf{F}(s)\mathbf{F}^{-1}(\tau)\mathbf{G}_{\text{pre}}^{i(\tau)}.$$

The fictitious, specific second Piola-Kirchhoff stress is usually computed from the strain energy per unit mass W^i with

$$\tilde{\mathbf{S}}^{i(\tau)} = 2 \frac{\partial W^i}{\partial \mathbf{F}_e^{i(\tau)}} : \frac{\partial \mathbf{F}_e^{i(\tau)}}{\partial \mathbf{C}}.$$

It is often assumed that the constituent is a fiber family that only creates stresses in one preferred direction and that newly deposited fibers are always aligned in the same direction [5, 6, 8, 11, 24, 25]. In that case, we can simplify equation (8) from a tensor equation to the scalar equation

$$\tilde{\sigma}^i(s) = \frac{1}{\kappa^i(s)} \left[q^{i(0)}(s)\tilde{\sigma}^{i(0)}(\lambda_e^{i(0)}) + \dots \right],$$

$$\int_0^s q^{i(\tau)}(s)\hat{\kappa}_+^i(\tau)\tilde{\sigma}^{i(\tau)}(\lambda_e^{i(\tau)})d\tau \Big],$$

where $\tilde{\sigma}^{i(\tau)}$ is the fictitious, specific fiber Cauchy stress, and $\lambda_e^{i(\tau)}$ is the total elastic stretch of the mass increment deposited at time τ . Initially, the total stretch of the fiber is $\lambda_e^{i(0)} = \lambda(s)\lambda_{\text{pre}}^{i(0)}$ and for later deposited increments, it is $\lambda_e^{i(\tau)} = \frac{\lambda(s)\lambda_{\text{pre}}^{i(\tau)}}{\lambda(\tau)}$, where $\lambda_{\text{pre}}^{i(\tau)}$ is the deposition stretch (prestretch) of the fiber. The fictitious, specific fiber Cauchy stress can be derived from the strain energy per unit mass via

$$\tilde{\sigma}^{i(\tau)} = \lambda \frac{\partial W^i}{\partial \lambda_e^{i(\tau)}} \frac{\partial \lambda_e^{i(\tau)}}{\partial \lambda} = \frac{\lambda \lambda_{\text{pre}}^{i(\tau)}}{\lambda(\tau)} \frac{\partial W^i}{\partial \lambda_e^{i(\tau)}}.$$

The fictitious, specific second Piola-Kirchhoff stress tensor can then be obtained with

$$\tilde{\mathbf{S}}^i(s) = \frac{\tilde{\sigma}^i(s)}{(\lambda(s))^2} \mathbf{f}_0^i \otimes \mathbf{f}_0^i.$$

Note that we use the second Piola-Kirchhoff stress tensor here so that we can use the constant reference fiber direction \mathbf{f}_0^i although the fibers rotate along the deformation.

Also note that the following adaptive integration strategy does not necessitate a scalar contribution of the stresses but can handle any tensorial quantity.

2.3 Adaptive history integration

The computationally expensive parts of constrained mixture models are the heredity integrals of the form

$$\int_0^s q^{i(\tau)} \mathcal{F}(\tau, s) d\tau \quad (9)$$

needed for the growth scalar (equation (7)) and the stress tensor (equation (8)). The possibly tensor-valued quantity \mathcal{F} represents tissue deposited into the mixture at the intermediate time τ . The integrand depends on the current deformation of the mixture and, therefore, has to be re-evaluated at every timestep, i.e., cannot be stored and reused from previous timesteps or Newton iterations.

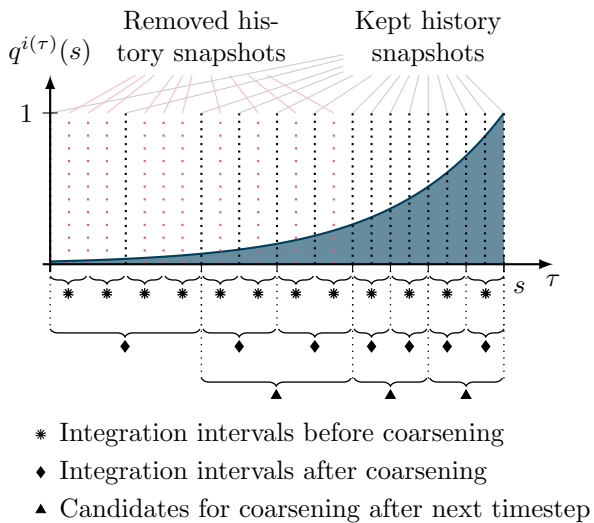


Fig. 2 Fraction of tissue deposited at time τ surviving at time s assuming a Poisson degradation process. With a non-adaptive G&R history integration, the history snapshots at the red and black dotted lines need to be stored. Since the influence of at time τ deposited mass increments on the current stress state decreases in time, the integration timestep can be adaptively increased while keeping the integration error constant. Each integration rule consists of three equally spaced history snapshots assuming a Simpson integration rule. Each two subsequent Simpson intervals with equal timestep size (marked with *) are combined if the condition of the adaptive strategy is fulfilled.

The evaluation of function $\mathcal{F}(\tau, s)$ requires information about the deformation state at intermediate times τ . Hence, the function can only be evaluated at points in time where the equilibrium (2) has been solved and stored. It is desirable to keep the number of stored configurations low to minimize the needed memory consumption in large 3D organ-scale simulations. Note that these are different needs than for classical adaptive quadrature rules, where one typically refines intervals to reduce the numerical error of the computation.

The function \mathcal{F} can be discontinuous in time. These discontinuities are typically imposed from the outside and known, e.g., discontinuous external loading. To keep the integration error low, we divide the integration domain $[0, s]$ into intervals where \mathcal{F} is continuous. Each interval is integrated by subsequently using the composed Newton-Cotes rule with three integration points

(Simpson's rule) [27]. In the first timestep, where only two history snapshots are available, two integration points are used (Trapezoidal rule) accordingly. We denote the numerical integration of function f in the interval \mathcal{I} using n Newton-Cotes integration points with $Q_n^{\mathcal{I}}(f)$. The integration rules are given in appendix A.

When using all history snapshots to integrate equation (9), the computational costs grow linearly in time. With the adaptive integration, we exploit that tissue is degraded over time following the survival function $q^{i(\tau)}$ (Figure 2). The influence of deposited mass increments on the mixture response decreases over time. The goal of the adaptive integration strategies is to keep the integration error constant over the interval $[0, s]$.

We denote the integration error on the interval \mathcal{I} of the numerical integration with $E_Q^{\mathcal{I}}$. Let us consider two consecutive Simpson intervals \mathcal{I}_1 and \mathcal{I}_2 with equal length Δs , each consisting of three history snapshots (see pairs marked with * in Figure 2). These two intervals are combined into a larger interval with length $2\Delta s$ if the numerical integration error on the larger interval, $E_Q^{\mathcal{I}_1+\mathcal{I}_2}$, is smaller than a tolerance. To keep the integration error constant over each subinterval, the allowed tolerance is scaled to the width of the combined interval, i.e., $\varepsilon_Q \frac{2\Delta s}{s}$, where ε_Q is the allowed tolerance for the whole integral from 0 to s . The condition for coarsening is, therefore,

$$E_Q^{\mathcal{I}_1+\mathcal{I}_2} \leq \varepsilon_Q \frac{2\Delta s}{s}. \quad (10)$$

The interior point of both integration intervals \mathcal{I}_1 and \mathcal{I}_2 are then removed from the history to free the memory. The resulting larger interval consists of three equally spaced snapshots where Simpson's rule can be applied again.

The integration error $E_Q^{\mathcal{I}}$ can, typically, not be determined analytically. We propose two different strategies to approximate this error. The first strategy assumes that the basal mass production rate is dominating G&R such that an analytical expression of the error can be derived. We call this strategy *model equation* adaptive strategy. The adaptive strategy is independent of the external loads such that the computational efforts can be estimated ahead of the simulation. The second strategy uses a higher-order integration rule to indicate the integration error with the benefit

that the additional error can be kept small even in cases with severe G&R. We call it *error indication* adaptive strategy.

2.3.1 Strategy A: Model equation

For the first strategy, we assume that the basal mass production in equation (5) is dominating G&R. In that case, the function $\mathcal{F}(\tau, s)$ can be reduced to $\mathcal{F}(\tau, s) = \frac{1}{T^i}$. If we further assume that degradation follows a Poisson process with a constant rate, the survival function $q^{i(\tau)}(s)$ can be pre-computed for each constituent, i.e.,

$$q^{i(\tau)}(s) = q^i(s - \tau),$$

where $q^i(\Delta s)$ is the fraction of mass still left after a timespan of Δs .

For this special case, the integral on an arbitrary subinterval $\mathcal{I} = [s_1, s_2]$ is

$$\int_{\mathcal{I}} q^i(s - \tau) \frac{1}{T^i} d\tau,$$

and can be computed analytically:

$$\int_{s_1}^{s_2} \frac{1}{T^i} \exp\left(-\frac{s - \tau}{T^i}\right) d\tau = \left[\exp\left(-\frac{s - s_2}{T^i}\right) - \exp\left(-\frac{s - s_1}{T^i}\right) \right].$$

The integration error of the model equation (see Figure 3 (a)) can then be expressed with

$$E_{\mathcal{Q}}^{\mathcal{I}} = \left| \mathcal{Q}_3^{\mathcal{I}}(q^i) - \int_{\mathcal{I}} \frac{1}{T^i} q^i d\tau \right|.$$

During pure maintenance (i.e., homeostasis), this exactly is the error of the integrals (7) and (8). However, the strategy does not see the amount of net mass production. As a consequence, the strategy might be too aggressive in freeing history snapshots in cases where net mass production dominates G&R. We denote this strategy with *model equation* adaptive strategy.

2.3.2 Strategy B: Error indication

In the second strategy, we approximate the analytical integration with a higher-order integration scheme. We have two subsequent Simpson intervals with the same timestep size Δs . Hence, five

quadrature points that are equally spaced can be used for integration, allowing to use Boole's integration rule (Newton-Cotes with 5 quadrature points) as depicted in Figure 3 (b). The approximated error is

$$E_{\mathcal{Q}}(\mathcal{I}) = \left| \mathcal{Q}_3^{\mathcal{I}}(\mathcal{G}) - \mathcal{Q}_5^{\mathcal{I}}(\mathcal{G}) \right|,$$

where \mathcal{G} is the full integrand, i.e.,

$$\mathcal{G} = q^{i(\tau)} \mathcal{F}(\tau, s).$$

This criterion does not rely on an analytical expression and can, therefore, be applied directly to the integrals occurring in constrained mixture models, namely equation (7) for the growth scalar and equation (8) for the Cauchy stress. The integral for the Cauchy stress is normalized with the homeostatic Cauchy stress to result in a dimensionless integral. The interval is coarsened if both errors are below the prescribed integration tolerances $\varepsilon_{\mathcal{Q}}^{\kappa}$ and $\varepsilon_{\mathcal{Q}}^{\sigma}$. We denote this strategy with *error indication* adaptive strategy.

2.4 Implementation

To model organ-scale G&R, the constrained mixture model is typically implemented in a finite element framework on the integration point level as a constitutive model that computes the stress given the deformation gradient. Algorithm 1 summarizes the principal steps of the model in such an environment.

In the element evaluation routine, the integrals of equations (7) and (8) have to be solved using the composite Simpson's rule. In case of a simple Poisson degradation process for the tissue, only the last snapshot in the integrals depends on the current stress response of the constituent via κ_+^i and equation (5). Hence, to solve the integral, a Newton-Raphson-type algorithm is applied locally. All older integration intervals can be integrated ahead of the local Newton-Raphson algorithm (Step 5 in Algorithm 1) to reduce computational costs. However, if tissue degradation depends on the current mechanobiological environment, reintegrating over the whole history in every local Newton-Raphson step is necessary. Once the growth scalar and the stress response are solved for each constituent, the stress response of the mixture can be computed with equation (1).

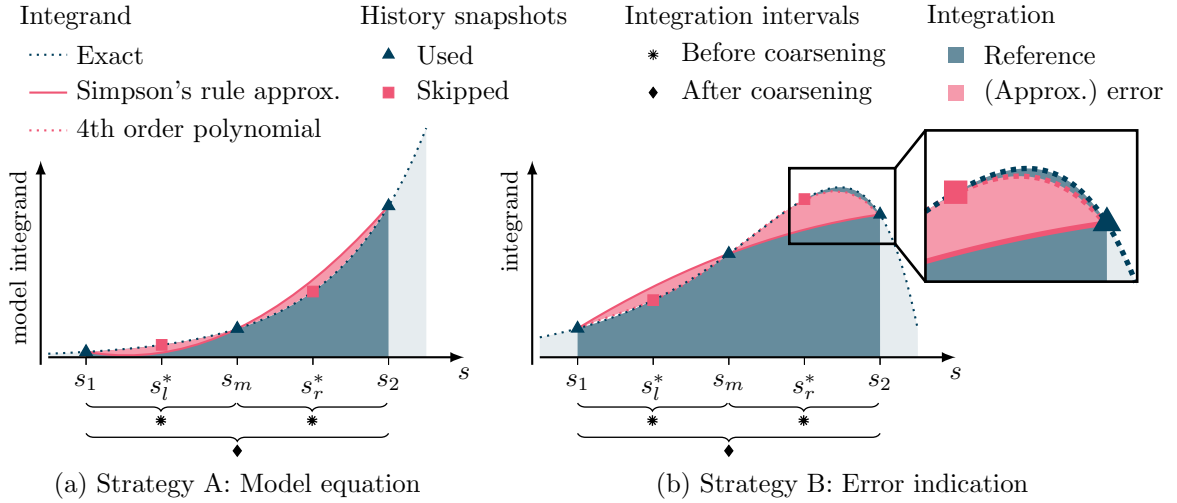


Fig. 3 Different strategies for coarsening the G&R history. (a) The integrands occurring in constrained mixture models are approximated by the model equation that only captures the continuous tissue decay. This integrand can usually be integrated analytically, so the integration error is computed based on the analytical solution. (b) The integration error for the integrals occurring in constrained mixture models is approximated with a higher-order Newton-Cotes integration rule using five integration points (i.e., using a fourth-order polynomial approximation). If the integration error is below a given tolerance, the history items marked with * are removed from the history, and the two Simpson intervals are combined.

After the equilibrium equation has been solved, the current states of the mass increments need to be added to the history. At this stage, older snapshots of the constrained mixture history can be removed according to the adaptive strategy (Step 13 in Algorithm 1) to free memory and reduce the computational costs of the following timesteps.

3 Quasi-1D Tissue patch example

As a first example, we consider a quasi-1D tissue patch, as shown in Figure 4. The tissue patch is loaded with a uniform traction with resulting force F in longitudinal direction. The support of the tissue patch is such that the stress response is uniform within the patch, and the equilibrium equation can be written as

$$\sigma - \frac{F}{A} = 0, \quad (11)$$

where A is the current cross-sectional area of the patch.

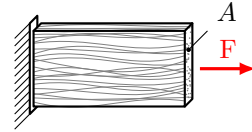


Fig. 4 The tissue patch with cross-sectional area A consisting of one fiber family aligned in the longitudinal direction. The external loading and the support of the patch is such that the stress response is homogeneous in the patch.

The tissue consists of a single family of Collagen fibers aligned in the longitudinal direction. New fibers are deposited in the same direction as extant fibers with the homeostatic prestretch λ_h . In case of unbalanced turnover, the tissue patch grows in cross-fiber direction such that the spatial mass density remains constant.

The collagen fibers are modeled with a Fung-type strain energy function per unit mass, i.e.,

$$W = \frac{a}{2b} \left\{ \exp \left[b(\lambda_e(\tau)^2 - 1)^2 \right] - 1 \right\}, \quad (12)$$

where a and b are material parameters. A Poisson degradation process, according to equation (4), continuously degrades fibers with the time

Algorithm 1 Implementation of a constrained mixture model with adaptive integration of history variables in a finite element framework.

```

1 Timestepping: While  $s < s_{\max}$ 
2   Newton-Raphson-like algorithm to solve (2)
3   Iterate over elements and Gauss points
4   Compute  $\mathbf{F}$ 
5   Solve  $\int_0^{s-\Delta s} \dots ds$  of (7) and (8)  $\forall i$ 
6   Newton-Raphson: Solve (7) and (8)  $\forall i$ 
7   Compute residuum and linearization
   of (7) and (8)
   Note: Reuse results from step 5
   if possible
8   Newton step: Update  $\kappa^i$  and  $\tilde{\mathbf{S}}^i$ 
9   Compute  $\mathbf{S}$  and linearization with (1)
10  Compute residuum of (2) and linearization
11  Newton step: Update displacements
12  Store configuration of all mass increments
13  Apply adaptive strategy (10)
14  Update G&R time  $s = s + \Delta s$ 

```

constant T . Mass is produced according to equation (6) with growth gain factor k_σ .

Initially, the tissue patch is loaded with F_0 such that the fibers, which are prestressed with λ_h , are in homeostasis. The loading scenario is shown in Figure 5. This homeostatic load is held for $20T$, where T is the mean survival time of the fiber. At $s = 20T$, the force is increased to $F = 10F_0$ and held constant for $20T$. Subsequently, the force is linearly ramped up to $20F_0$ within $20T$ and kept constant for $40T$. Finally, the baseline value F_0 of the force is restored and kept for $40T$. This scenario ensures that the adaptive strategies are tested for different loading aspects that can occur in-vivo, like homeostatic loading, a sudden and continuous load increase, and a reverse G&R phase.

The parameters used for the simulations are given in Table 1. We integrate the problem with a timestep size of $\Delta s = 0.75$ days, which is a twentieth of the time constant T . We compare the results using both adaptive strategies and tolerances of

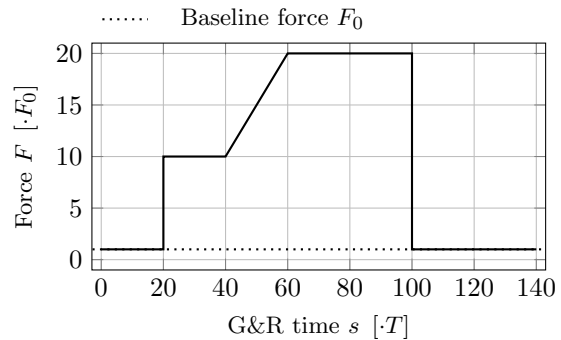


Fig. 5 The loading scenario of the patch. F_0 is the initial force such that the patch is in homeostasis, and T is the time-constant of the Poisson degradation process of the tissue.

Table 1 Material parameters for the fibers of the tissue patch. Material parameters are taken from Braeu et al. [5].

Name	Parameter	Value
<i>Collagen parameters</i>		
Fung exponential parameters	a	568 J/kg
	b	11.2
<i>Homeostatic stretches</i>		
Homeostatic stretch	λ_h	1.062
<i>G&R parameters</i>		
Mean survival time	T	15 days
Growth gain	k_σ	$0.1/T$

$\varepsilon_Q^\kappa = \varepsilon_Q^\sigma = \varepsilon_Q \in \{10^{-4}, 10^{-5}, \dots, 10^{-9}\}$ with non-adaptive history integration. The reference solution is obtained with a non-adaptive history integration with ten times smaller timestep size.

Figure 6 compares the two adaptive strategies with different adaptive tolerances. The first two rows (relative Cauchy stress error and relative patch mass error) result directly from the two integrals occurring in constrained mixture models, i.e., equations (8) and (7), respectively.

The relative errors can, naturally, not be smaller than for the full integration case. During the initial maintenance phase, the relative error of the full integration is at around 10^{-6} for the Cauchy stress and the patch mass. The errors of the adaptive integrations are on the same level except for those cases with a higher adaptive tolerance. In the subsequent phases of G&R, the relative errors of the full integration and the error indication adaptive strategy are on the same level. The relative error is higher for the model

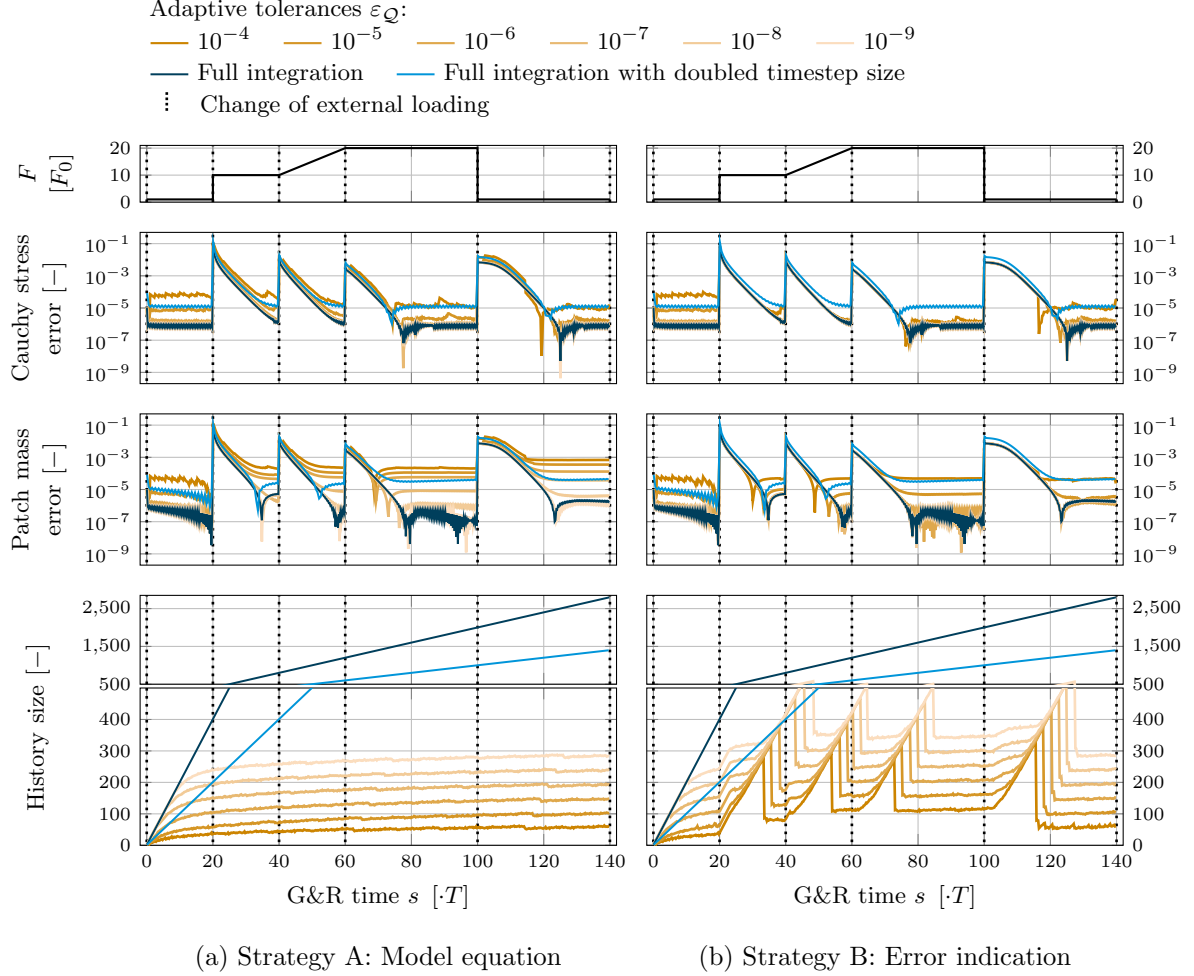


Fig. 6 Relative Cauchy stress error, relative patch mass error, and the history size for the quasi-1D patch example integrated with the (a) model equation adaptive strategy and (b) error indication adaptive strategy and with a full integration. The reference solution is computed with full integration and a tenth of the timestep size.

equation adaptive theory, especially when using loose adaptive tolerances.

It is important to note that the relative error of the Cauchy stress can recover the initial level after a longer phase of constant load as the Cauchy stress converges (in mechanobiologically stable G&R) towards the homeostatic stress. However, the relative patch mass error tends to accumulate over time as this quantity is not a mechanobiologically controlled variable. This is especially pronounced for the model equation adaptive strategy with loose adaptive tolerances, where the relative errors are larger.

The last row of Figure 6 shows the number of snapshots that are stored in the history. The

history size correlates directly with the computational costs of the model, i.e., the needed memory consumption and the evaluation time. The number of snapshots in the history for the model equation adaptive strategy is independent of the load and can be computed ahead of time. When using the error indication strategy, the history size increases after changes in the external load, resulting in changing memory demands depending on the external loading. The peak history size for the strictest analyzed tolerance ($\varepsilon_Q = 10^{-9}$) is below 300 for the model equation adaptive strategy and around 500 for error indication adaptive strategy. Both strategies need significantly fewer stored snapshots than the full integration with about 2800 stored snapshots. This difference is

even more pronounced for looser adaptive tolerances. Since the history size increases linearly for the full integration and plateaus for both adaptive strategies, the reduction of computational costs will become even more drastic when advancing further in time.

In Figure 6, we added a fully integrated case with a doubled timestep size for comparison (light blue). The total error is on the same level as the adaptive integration with the largest tolerance. However, the final history size, which strongly correlates with evaluation time and memory consumption, is larger by a factor of around 23 with a tendency to increase further with the simulation time.

4 3D cardiac example

To demonstrate that the adaptive integration enables organ-scale simulations of constrained mixture models, we apply it to a patient-specific model of the two ventricles. The geometry is segmented from MRI data of a healthy female subject. Following Gebauer et al. [11], we use the data from the end-systolic configuration. We use a mesh with 67412 second-order tetrahedral elements generated with Gmsh [12] depicted in Figure 7. We use a Newton algorithm with backtracking for solving the nonlinear equilibrium equations and a conjugate gradient method for linear systems [31] implemented in our in-house research code 4C [1] written in C++.

4.1 Modeling

We apply different boundary conditions on the surfaces defined in Figure 7. The influence of the pericardial sac on the epicardium is modeled with a Robin boundary condition [26] in reference surface normal direction on the surface Γ_{epi} with linear spring stiffness c_p . On the basal surface Γ_b , omnidirectional Robin boundary conditions with linear spring stiffness c_b mimic the support of the atria and adipose tissue. The blood in both ventricles is modeled with a pressure boundary condition of the endocardia of the left- and right ventricle (Γ_{lv} and Γ_{rv}) with blood pressure values p_{lv} and p_{rv} , respectively. The resulting virtual

■ Epicardium Γ_{epi} ■ Left endocardium Γ_{lv}
 ■ Base Γ_b ■ Right endocardium Γ_{rv}



Fig. 7 The patient-specific model of ventricles of a healthy female subject. The color represents the surfaces where different boundary conditions are applied.

work formulation is

$$\begin{aligned} \delta W &= \frac{1}{2} \int_{B_0} \mathbf{S} : \delta \mathbf{C} \, dV \\ &+ \int_{\Gamma_{\text{epi}}} (c_p \mathbf{u} \cdot \mathbf{N}_0) \delta \mathbf{u} \, d\Gamma + \int_{\Gamma_b} c_b \mathbf{u} \delta \mathbf{u} \, d\Gamma \\ &+ \int_{\Gamma_{\text{lv}}} p_{\text{lv}} J \mathbf{F}^{-T} \mathbf{N}_0 \, d\Gamma + \int_{\Gamma_{\text{rv}}} p_{\text{rv}} J \mathbf{F}^{-T} \mathbf{N}_0 \, d\Gamma \\ &= 0, \end{aligned}$$

where \mathbf{N}_0 is the outward reference surface normal.

We follow Gebauer et al. [11] for modeling the constituents of the myocardium. That are cardiomyocytes ($i = m$) and 4 Collagen fiber families ($i = c$), all modeled as quasi-1D constituents and computed for the patient-specific geometry with a rule-based algorithm [4] by prescribing the helix angle φ at the endo- and epicardium. The remaining constituents (mainly elastin) are combined in an isotropic constituent ($i = 3D$). During adulthood, no functional elastin is deposited into the matrix. Hence, we assume that the isotropic constituent does not turnover ($k^{3D} = 0$, $T^{3D} \rightarrow \infty$).

The strain energy per unit mass of collagen fibers in the direction \mathbf{f}^{c_i} are modeled with a Fung exponential strain energy function, analogously to equation (12), with material parameters a^c and b^c .

The strain energy function of cardiomyocytes additively splits into a passive and active contribution:

$$W^m = W_{\text{pas}}^m + W_{\text{act}}^m.$$

As with the collagen fibers, the strain energy function per unit mass for the passive response of cardiomyocytes is a Fung exponential strain energy function with material parameters a^m and b^m . The active contribution is

$$W_{\text{act}}^m = \frac{\sigma_{\text{act}}^m}{\rho_0 s = 0} \left[\lambda_{\text{act}}^m + \frac{1}{3} \frac{(\lambda_{\text{max}}^m - \lambda_{\text{act}}^m)^3}{(\lambda_0^m)^2} \right],$$

with $\frac{\partial \lambda_{\text{act}}^m}{\partial \lambda_{\text{act}}^m(\tau)} = \frac{1}{\lambda_{\text{act}}^m(\tau)}$ [6, 34].

The strain energy function per unit mass of the remaining constituents is an isotropic neo-Hookean strain energy contribution of the form

$$W^{3D} = c_1(\bar{I}_1 - 3),$$

where \bar{I}_1 is the first modified invariant [13] of the total elastic Cauchy-Green deformation tensor with the isotropic and rotation-free prestretch tensor \mathbf{G}^{3D} . The latter maps the stress-free configuration of elastin into the reference configuration.

We follow Braeu et al. [6] to model anisotropic growth of the tissue. They describe growth by an elastic swelling of all existing constituents with a modified penalty formulation. The additional term of the strain energy function is

$$\Psi^\# = \frac{\kappa}{2} \left(|\mathbf{F}| - \frac{\rho_0(s)}{\rho_0(s=0)} \right)^2,$$

where κ is a penalty parameter. A sufficiently high penalty parameter ensures a constant spatial density of the mixture. The resulting tissue growth is anisotropic and happens mainly in the direction of the smallest stiffness. A key advantage of that theory is that the anisotropy of G&R naturally emerges from the anisotropic stiffness of the tissue and does not rely on a phenomenological definition of a growth tensor. Note that our adaptive integration strategies can also be combined with inelastic growth laws.

4.2 Loading scenario

The configuration obtained from MRI data is not stress-free in the depicted configuration. Since the data is from a healthy subject, we assume the configuration is in homeostasis, i.e., all fiber constituents are in their preferred mechanical state. The baseline blood pressure in the left and right ventricle is given by p_{lv} and p_{rv} , respectively.

We apply the prestress algorithm presented in Gebauer et al. [11] until the maximum Euclidean norm of the nodal displacements falls below ε_{pre} to ensure that the initial configuration is close to the reference (imaged) configuration. The subsequent phase of G&R of 200 days with blood pressure levels remaining at baseline ensure mechanobiological equilibrium of all constituents.

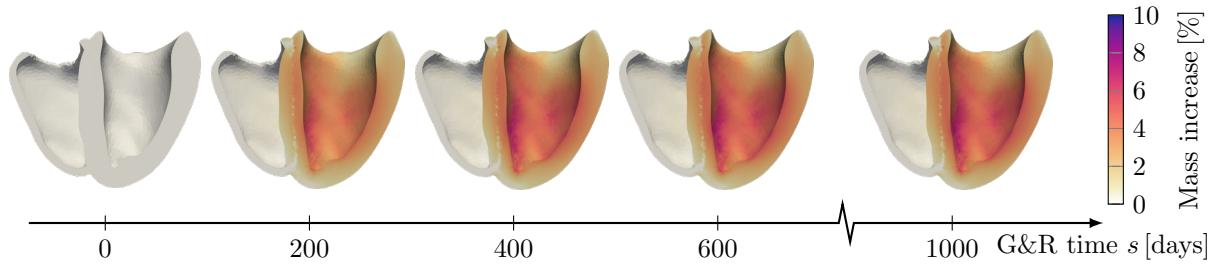
We simulate two hypertension conditions by elevating the left ventricular pressure at $s = 0$ to $p_{\text{lv}}^+ = 140$ mmHg and $p_{\text{lv}}^+ = 180$ mmHg. The resulting G&R are mechanobiologically stable and unstable, respectively.

4.3 Results

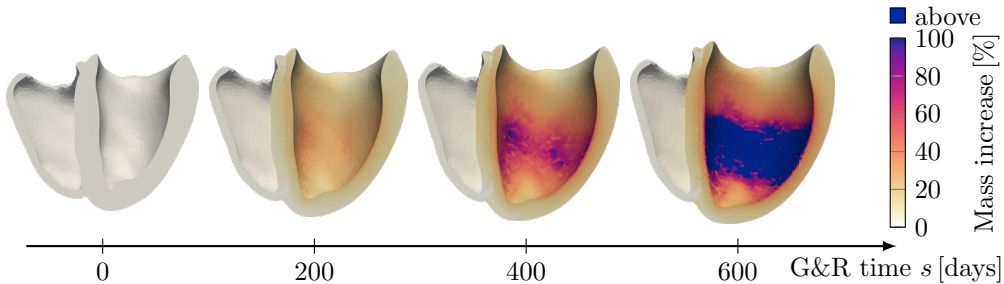
Table 2 shows the material and simulation parameters used for the organ-scale example. The mechanobiologically stable case ran for 1000 days and the mechanobiologically unstable case for 600 days. The baseline timestep size is $\Delta s = 0.5$ days, which is a twentieth of the minimum involved turnover time constant.

Figure 8 shows the resulting G&R after increasing the left ventricular pressure for both loading scenarios. In the mechanobiological stable loading scenario, the maximum mass increase occurs at the endocardium of the left ventricle and is around 6%, resulting in a configuration that is in mechanobiological equilibrium. The mechanobiological unstable loading scenario does not result in a mechanobiological equilibrated state within the considered timeframe. The maximum local mass increase is 130% after 600 days of unstable G&R continuing to increase over time.

We ran the mechanobiologically stable and unstable loading cases for each adaptive strategy and with a full history integration for comparison. As a reference solution, we additionally ran the full integration case with a halved timestep size to compare the adaptive strategy errors with the full integration. Halving the timestep size reduces the integration error of Simpson's rule by a factor of $\frac{1}{32}$ [19], allowing to indicate the integration error with a meaningful precision. A further reduction of the timestep size is infeasible for the 3D organ-scale example since the computation time of the full integration case increases quadratically, and memory consumption increases linearly with the number of timesteps.



(a) Mechanobiologically stable G&R



(b) Mechanobiologically unstable G&R

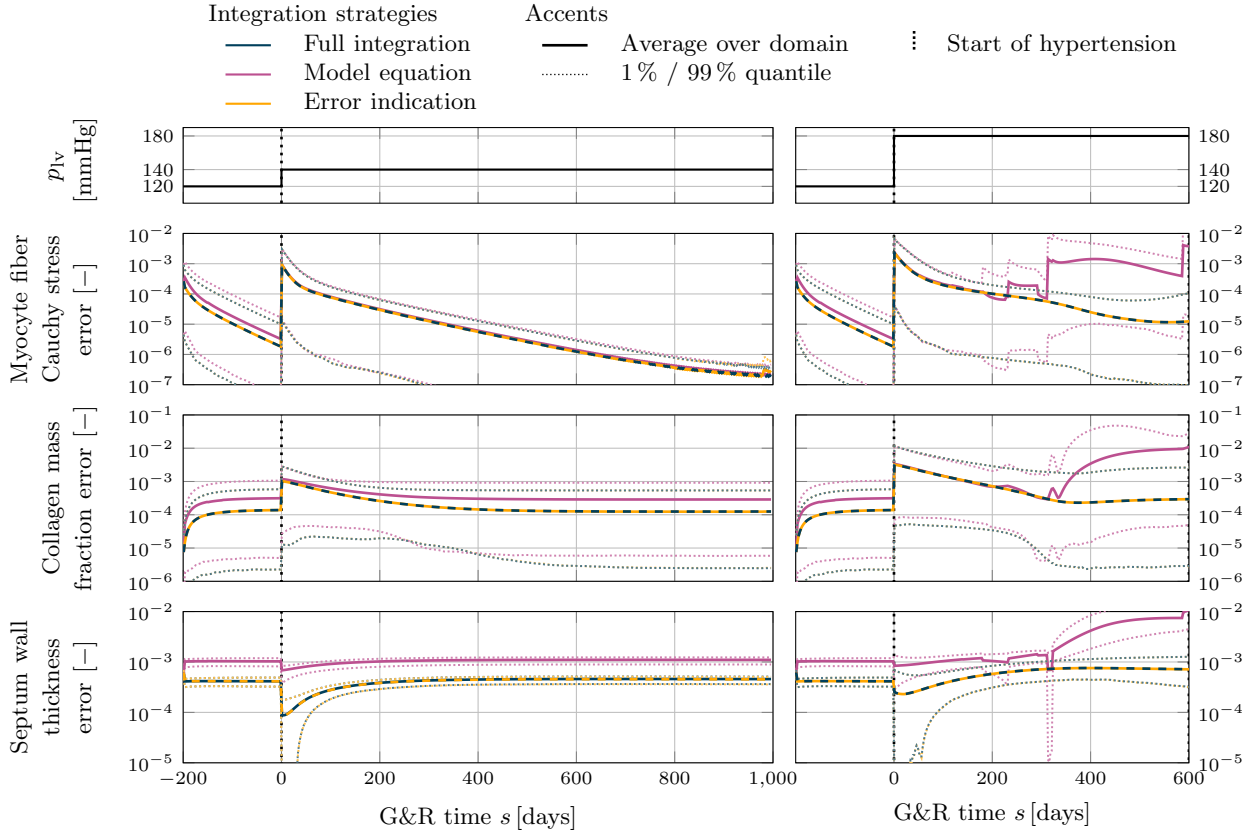
Fig. 8 Local mass increase at different times in the myocardium for (a) mechanobiologically stable and (b) unstable G&R. The results stem from the full integration case with baseline timestep size. The differences to the other considered cases are negligibly small.

Figure 9 shows the relative errors of the myocyte fiber Cauchy stress, collagen mass fraction, and the wall thickness of the septum of the considered cases. The Cauchy stress and the mass fraction are evaluated at each integration point. The wall thickness of the septum is computed for every node on the endocardium of the septum and compared to the reference simulation. All those quantities are shown as average over the domain, and spatial inhomogeneities are indicated with the 1% / 99% quantiles of each quantity.

The model equation adaptive strategy can only partially reproduce the results of the full integration. The error is especially pronounced in the late phase of mechanobiologically unstable G&R dominated by the adaptive integration. In contrast, the error indication adaptive strategy can reproduce the results of the full integration for both loading scenarios. Even at the end-stage of severe G&R, the additional error of local and global quantities with both adaptive strategies are small such that they can typically be neglected compared to other errors in mechanobiological models.

Figure 10 shows the history size and the Newton step solution time. The history size is the sum of the snapshots of all constituents stored at each integration point.

The history size of the full integration increases linearly since one snapshot is stored for each constituent and timestep. At $s = 1000$ days, i.e., after 2400 timesteps, this results in a history size of $12 \cdot 10^3$ snapshots per quadrature point of the finite element discretization. Like the history size, the Newton step solution time also increases linearly. The model equation adaptive theory is independent of the load, resulting in the same history size in the myocardium for mechanobiologically stable and unstable G&R. It plateaus at around 1000 history snapshots with the consequence that the computational costs also remain almost constant in time (cf., Newton step solution time). When using the error indication adaptive strategy, the history size depends on the local mechanobiological environment and is, therefore, locally inhomogeneous and different for mechanobiologically stable and unstable G&R. The final history size



(a) Mechanobiologically stable G&R (b) Mechanobiologically unstable G&R

Fig. 9 Relative errors of the myocyte fiber Cauchy stress, collagen mass fraction, and septum wall thickness for full history integration, model equation adaptive strategy with adaptive tolerance $\varepsilon_Q = 10^{-9}$ and error indication adaptive strategy with adaptive tolerance $\varepsilon_Q = 10^{-5}$ for the 3D organ-scale example. The left ventricular pressure is increased at $s = 0$ from baseline 120 mmHg to (a) 140 mmHg for mechanobiological stable and (b) 180 mmHg for mechanobiological unstable G&R.

is also approximately 1000 history snapshots with an almost constant Newton step solution time.

Figure 11 shows the relative septum wall thickness error and the average history size at G&R time $s = 600$ days for different adaptive tolerances ε_Q . Note that the septum wall thickness is an organ-scale quantity and not mechanobiologically regulated, i.e., the errors in this quantity accumulate over time.

The full history integration defines the lower bound of the relative septum wall thickness error. The error indication adaptive strategy reaches the lower bound with an adaptive tolerance of 10^{-5} for both loading scenarios. Reducing the adaptive tolerance does not further reduce the wall thickness error since the base timestep size dominates the error. It is just a coincidence that the

error of the mechanobiological unstable G&R case is slightly below the lower bound. The error of the model equation adaptive strategy is higher than that of the error indication adaptive strategy. An adaptive tolerance of 10^{-11} is needed for the mechanobiologically stable G&R scenario to reduce the error to the lower bound. For the mechanobiologically unstable G&R scenario, the model equation adaptive strategy cannot reduce the error to the lower bound within the considered tolerance range.

It is important to note that to decrease the integration error below the lower bound defined by the full integration, it is necessary to decrease the base timestep size of the integration.

The average history sizes of both adaptive strategies in Figure 11 are roughly on a straight

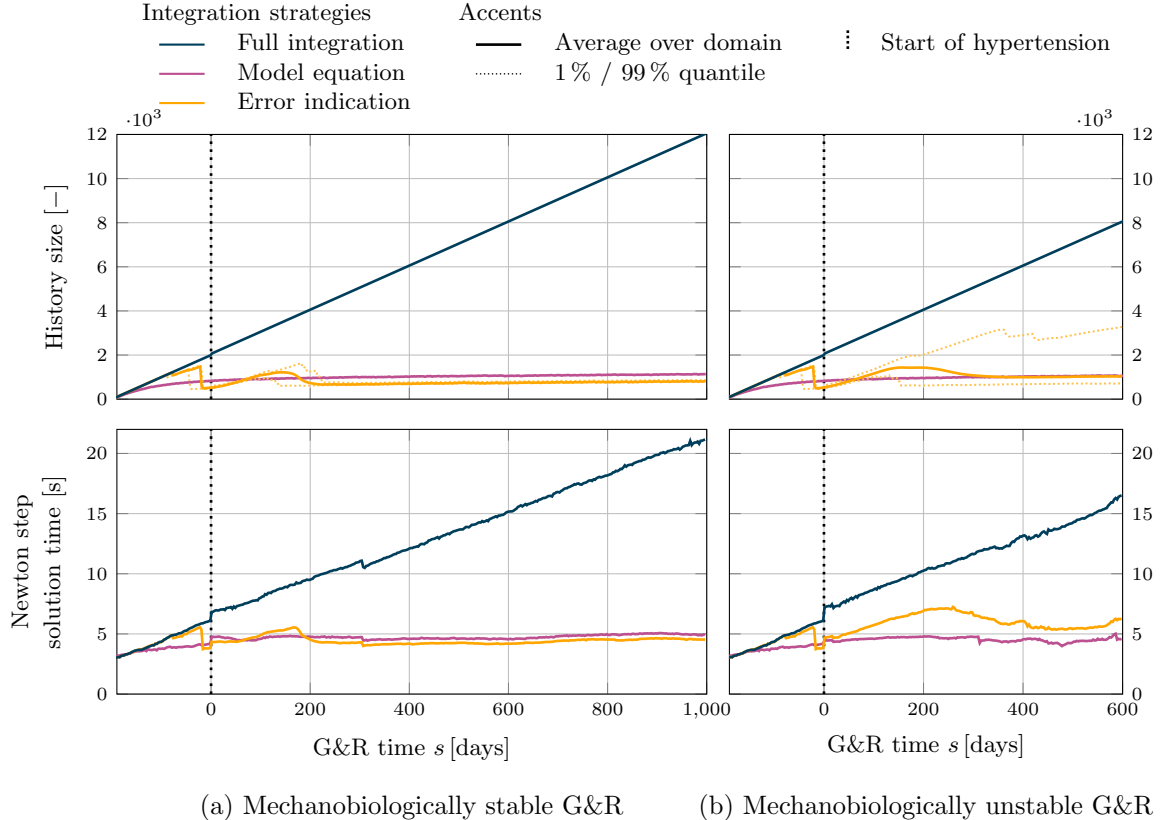


Fig. 10 History size and Newton step solution time of the 3D organ-scale example using full history integration, the model equation adaptive strategy with adaptive tolerance $\varepsilon_Q = 10^{-9}$ and error indication adaptive strategy with adaptive tolerance $\varepsilon_Q = 10^{-5}$ (cf. Figure 9). The pressure in the left ventricle is elevated from baseline 120 mmHg to (a) 140 mmHg (mechanobiologically stable G&R) and (b) 180 mmHg (mechanobiologically unstable G&R).

line on the semilogarithmic plot with similar slope. Reducing the tolerance by a factor of 10^{-1} results in a history size that is larger by around 300 – 400 snapshots. The average history size is smaller for the model equation adaptive strategy with the same adaptive tolerance compared to the error indication adaptive strategy. In the latter, unstable G&R also results in a larger history size than for stable G&R. Even for very small tolerances, the average history size is significantly smaller compared to the full history integration case.

5 Discussion

We presented two strategies to adaptively integrate the history variables in constrained mixture models with the goal of drastically reducing the computational effort of such models. The strategies exploit the fact that the influence of tissue

once deposited decreases over time through degradation. We analyzed the strategies on a tissue patch in reduced dimensions and demonstrated that both strategies enable the simulation of long-running G&R models while keeping the error in both local and global quantities below physiological relevant scales on a level comparable to the full integration.

5.1 Strategy A: Model equation

We presented a strategy that adapts the history integration by approximating the error with analytical solution during tissue maintenance. The strategy does not take into account the additional mass deposition if the tissue is not in homeostasis.

This method should be the method of choice if it is particularly important to predict the computational costs of the model evaluation in advance. The history size only depends on the timestep size,

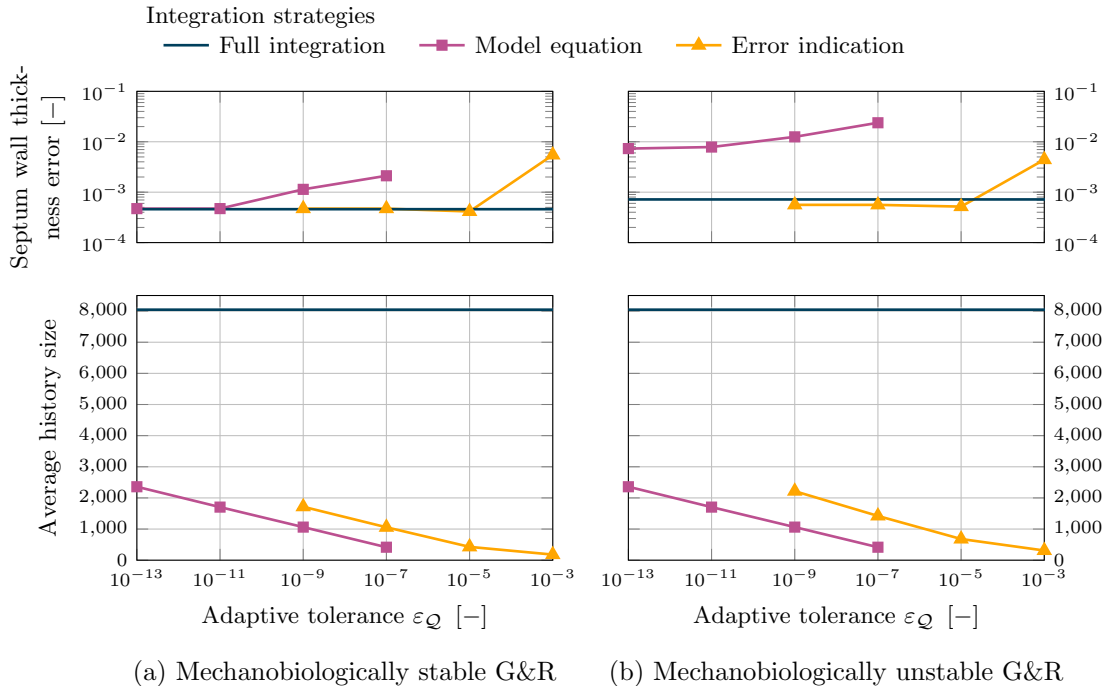


Fig. 11 Relative septum wall thickness error and history size for the organ-scale example using different adaptive tolerances at the time $s = 600$ days for the (a) mechanobiologically stable and (b) mechanobiologically unstable loading scenario.

the degradation time constant, and the adaptive tolerance and can, therefore, typically be computed ahead of the simulation. This comes with the downside that the additional integration error is generally larger than the prescribed adaptive tolerance for severe G&R scenarios.

5.2 Strategy B: Error indication

We also presented a strategy that uses a higher-order numerical integration scheme to compute the error. This strategy uses the actual integrals that need to be solved in constrained mixture models. As a result, the history size is spatially inhomogeneous, i.e., parts with higher mass deposition store more history snapshots than those with less dominant mass deposition. The available computing resources can, therefore, be optimally used. The adaptive tolerance directly controls the additional error in local G&R quantities and as a consequence, also organ-scale quantities. This makes this adaptive strategy particularly useful for severe G&R.

A downside of the adaptive strategy is that it is hardly possible to compute the history size ahead of the simulation time. It is, therefore, difficult to

estimate the needed computational resources (e.g., the amount of needed peak memory).

5.3 Computational costs

We ran each simulation on one node of our in-house Linux cluster with AMD Epyc 9354 Zen 4 with 384 GB RAM and 32 cores at 3.25 GHz. The non-adaptive history integration needed for mechanobiological stable G&R 253 GB RAM, compared to 39 GB for error indication and for model equation adaptive strategy. The total simulation time for the 1000 days period of stable G&R was 31 h for the non-adaptive case compared to around 10 h for the model equation and error indication adaptive strategy.

Both simulation time and memory consumption correlate with the number of snapshots in the history. With our adaptive strategies, the history size plateaus and remains fairly constant afterward, i.e., the computational complexity of the memory requirements is $\mathcal{O}(1)$ with the number of timesteps. As a consequence, the solution time of one timestep is also constant in time. Hence, solving n timesteps has a computation time complexity of $\mathcal{O}(n)$ as typically expected from a

Table 2 Material and Simulation parameters used for the 3D organ-scale example. The parameters are adopted from Braeu et al. [5] and Gebauer et al. [11].

Name	Param.	Value
<i>Fibers</i>		
Epicardial fiber helix angle	φ_{epi}	-60°
Endocardial fiber helix angle	φ_{endo}	60°
<i>Material parameters</i>		
Myocytes:		
Fung exponential parameters	a^m	7.6 J/kg
	b^m	11.4
Active muscle tone	σ_{act}^m	54 kPa
	λ_0^m	0.8
	λ_{max}^m	1.4
Collagen:		
Fung exponential parameters	a^c	568 J/kg
	b^c	11.2
Elastin matrix:		
Neo-Hookean parameter	a^e	72 J/kg
Volumetric penalty	κ	150 kPa
<i>Boundary conditions</i>		
Spring stiffness:		
Base	c_{base}	2.0 Pa/mm
Pericardium	c_p	0.2 Pa/mm
Baseline pressure:		
Left ventricle	p_{lv}	120 mmHg
Right ventricle	p_{rv}	24 mmHg
Elevated left ventricular pressure:		
Stable G&R	p_{lv}^+	140 mmHg
Unstable G&R	p_{lv}^+	180 mmHg
<i>Initial conditions</i>		
Reference mass density	ρ_0	1050 kg/m ³
Myocyte mass fraction	ξ^m	0.6
Collagen mass fraction	ξ^c	0.1
Elastin mass fraction	ξ^e	0.3
<i>G&R parameters</i>		
Myocytes:		
Homeostatic stretch	λ_h^m	1.1
Growth gain	k^m	$0.1/T^m$
Sarcomere mean survival time	T^m	10 days
Collagen:		
Homeostatic stretch	λ_h^c	1.062
Growth gain	k^c	$0.1/T^c$
Mean survival time	T^c	15 days
<i>Adaptive tolerance</i>		
Model equation	ε_Q	10^{-9}
Error indication	ε_Q	10^{-5}
<i>Prestressing</i>		
Prestress tolerance	ε_{pre}	0.01 mm

transient problem. For the non-adaptive simulation, the memory consumption and the timestep solution time grow linearly with the number of timesteps, resulting in a computation time complexity of $\mathcal{O}(n^2)$, hence eventually reaching the boundary of any computing hardware in terms of memory consumption and evaluation time. To compare the simulation results, we limited our

organ-scale example to be small enough to evaluate it with the non-adaptive integration. Larger meshes or longer G&R periods, e.g., needed for studying mechanobiological stability or reversal, quickly make the non-adaptive integration infeasible.

With our choice of tolerances, the increase of the evaluation time in the adaptive cases remains smaller than the solution time of the iterative linear solver. Hence, the model solution time is dominated by the linear solver. The evaluation of the whole model remains, therefore, comparable to models that just integrate local ordinary differential equations, like homogenized constrained mixture models [8] and kinematic growth models [28].

5.4 Limitations

The topic of this paper was the introduction and investigation of two approaches to control the *additional* error of the adaptive integration. One needs to keep in mind that this is not the total integration error. The latter is controlled by the timestep, which should be small enough to ensure that the integration error is below physiological relevant scales. The adaptive tolerance should be chosen small enough to ensure that the *additional* error of the adaptive integration is negligible in organ-scale G&R results. This is particularly important since organ-scale quantities like the wall thickness, lumen, or organ mass are not directly mechanobiologically controlled, and errors made during model evaluation accumulate over time.

For simplicity, we assumed a simple Poisson degradation process for the tissue constituents. However, processes leading to cell apoptosis and tissue degradation are generally complex and can depend on the current mechanobiological environment. Adaptive integration of the history variables can still result in a significant reduction of computational costs, especially when using the error indication adaptive strategy, which naturally can handle any degradation rules.

In our implementation, we assume that constituents that do turnover are fibers that only contribute to the mixture stress in their preferred direction and that new fibers are deposited in the same direction [5, 6, 11, 24, 25]. This is not a limitation of the proposed adaptive integration

strategies. We expect similar speedup results for an implementation of a general 3D constituent with turnover following equation (8). That allows modeling fiber reorientation due to G&R and also enables fiber dispersion models [10] for predicting increased dispersion during disease progression [9].

In our model, the driving factor of G&R is the difference in the Cauchy-stress of the constituent. However, other G&R stimuli like wall shear stress in blood vessels [15, 29] or infiltration of inflammatory cells [15, 18, 21] also play an important role in soft tissue G&R. Our adaptive strategies should also capture these cases, especially the error indication adaptive strategy where additional stimuli are directly considered during adaption.

A Newton-Cotes integration rules

The global time-stepping of the finite element framework often results in equidistant timesteps. To integrate the history variables in constrained mixture models, closed Newton-Cotes integration rules, i.e., integration rules with equidistant quadrature points need to be used. We denote the Newton-Cotes integration of the function \mathcal{F} with n points on the interval $\mathcal{I} = [a, b]$ with $Q_n^{\mathcal{I}}(\mathcal{F})$. The equidistant quadrature points are at

$$s_i = a + (i - 1) \frac{b - a}{n - 1}, \quad i = 1, 2, \dots, n$$

and the function \mathcal{F} evaluated at s_i is denoted as \mathcal{F}_i .

The trapezoidal rule [19] uses just the endpoints of the interval that we use in the first timestep where only two snapshots are available. The quadrature is given as

$$Q_2^{\mathcal{I}}(\mathcal{F}) = \frac{b - a}{2} (\mathcal{F}_1 + \mathcal{F}_2).$$

Typically, during integration, we apply the composite Simpson's rule [19] with an additional midpoint, i.e.,

$$Q_3^{\mathcal{I}}(\mathcal{F}) = \frac{b - a}{6} (\mathcal{F}_1 + 4\mathcal{F}_2 + \mathcal{F}_3).$$

The Boole's integration [19] is used to approximate the integration error to adaptively integrate

the G&R history. The quadrature rule is

$$Q_5^{\mathcal{I}}(\mathcal{F}) = \frac{b - a}{90} (7\mathcal{F}_1 + 32\mathcal{F}_2 + 12\mathcal{F}_3 + 32\mathcal{F}_4 + 7\mathcal{F}_5).$$

Declarations

Author contributions. AMG was involved in conceptualization, methodology, software, validation visualization, and original draft writing. MRP contributed to methodology, validation, visualization, and draft review and editing. JMS was involved in validation, visualization, and reviewing and editing the draft. WAW contributed to conceptualization, funding acquisition, resources, supervision, and draft review and editing.

Funding. MRP was supported by the National Heart, Lung, and Blood Institute of the National Institutes of Health under Award Number K99HL161313 and the Stanford Maternal and Child Health Institute. The content is solely the responsibility of the authors and does not represent the official views of the National Institutes of Health. WAW acknowledges the support by BREATHE, a Horizon 2020-ERC-2020-ADG project, grant agreement No. 101021526-BREATHE.

Conflict of interest. The authors declare that they have no competing interests.

Ethical approval. not applicable

References

- [1] 4C (2024) 4C: A Comprehensive Multi-Physics Simulation Framework. <https://www.4c-multiphysics.org>, accessed: March 27, 2024
- [2] Baek S, Rajagopal KR, Humphrey JD (2006) A Theoretical Model of Enlarging Intracranial Fusiform Aneurysms. *Journal of Biomechanical Engineering* 128(1):142–149. <https://doi.org/10.1115/1.2132374>
- [3] Baek S, Valentín A, Humphrey JD (2007) Biochemomechanics of Cerebral Vasospasm and its Resolution: II. Constitutive Relations and Model Simulations. *Annals of Biomedical Engineering* 35(9):1498. <https://doi.org/10.1007/s10439-007-9322-x>

- [4] Bayer JD, Blake RC, Plank G, et al. (2012) A Novel Rule-Based Algorithm for Assigning Myocardial Fiber Orientation to Computational Heart Models. *Annals of Biomedical Engineering* 40(10):2243–2254. <https://doi.org/10.1007/s10439-012-0593-5>
- [5] Braeu FA, Seitz A, Aydin RC, et al. (2016) Homogenized constrained mixture models for anisotropic volumetric growth and remodeling. *Biomechanics and Modeling in Mechanobiology* 16(3):889–906. <https://doi.org/10.1007/s10237-016-0859-1>
- [6] Braeu FA, Aydin RC, Cyron CJ (2019) Anisotropic stiffness and tensional homeostasis induce a natural anisotropy of volumetric growth and remodeling in soft biological tissues. *Biomechanics and Modeling in Mechanobiology* 18(2):327–345. <https://doi.org/10.1007/s10237-018-1084-x>
- [7] Cyron CJ, Humphrey JD (2017) Growth and remodeling of load-bearing biological soft tissues. *Meccanica* 52(3):645–664. <https://doi.org/10.1007/s11012-016-0472-5>
- [8] Cyron CJ, Aydin RC, Humphrey JD (2016) A homogenized constrained mixture (and mechanical analog) model for growth and remodeling of soft tissue. *Biomechanics and Modeling in Mechanobiology* 15(6):1389–1403. <https://doi.org/10.1007/s10237-016-0770-9>
- [9] Eriksson TSE, Prassl AJ, Plank G, et al. (2013) Modeling the dispersion in electromechanically coupled myocardium: MODELING THE DISPERSION IN ELECTROMECHANICALLY COUPLED MYOCARDIUM. *International Journal for Numerical Methods in Biomedical Engineering* 29(11):1267–1284. <https://doi.org/10.1002/cnm.2575>
- [10] Gasser TC, Ogden RW, Holzapfel GA (2006) Hyperelastic modelling of arterial layers with distributed collagen fibre orientations. *Journal of The Royal Society Interface* 3(6):15–35. <https://doi.org/10.1098/rsif.2005.0073>
- [11] Gebauer AM, Pfaller MR, Braeu FA, et al. (2023) A homogenized constrained mixture model of cardiac growth and remodeling: analyzing mechanobiological stability and reversal. *Biomechanics and Modeling in Mechanobiology* pp 1–20. <https://doi.org/10.1007/s10237-023-01747-w>
- [12] Geuzaine C, Remacle J (2009) Gmsh: A 3-D finite element mesh generator with built-in pre- and post-processing facilities. *International Journal for Numerical Methods in Engineering* 79(11):1309–1331. <https://doi.org/10.1002/nme.2579>
- [13] Holzapfel GA (2000) *Nonlinear Solid Mechanics: A Continuum Approach for Engineering*. Wiley
- [14] Horvat N, Virag L, Holzapfel GA, et al. (2019) A finite element implementation of a growth and remodeling model for soft biological tissues: Verification and application to abdominal aortic aneurysms. *Computer Methods in Applied Mechanics and Engineering* 352:586–605. <https://doi.org/10.1016/j.cma.2019.04.041>
- [15] Humphrey JD (2008) Vascular Adaptation and Mechanical Homeostasis at Tissue, Cellular, and Sub-cellular Levels. *Cell Biochemistry and Biophysics* 50(2):53–78. <https://doi.org/10.1007/s12013-007-9002-3>
- [16] Humphrey JD (2021) Constrained Mixture Models of Soft Tissue Growth and Remodeling – Twenty Years After. *Journal of Elasticity* pp 1–27. <https://doi.org/10.1007/s10659-020-09809-1>
- [17] Humphrey JD, Rajagopal KR (2002) A constrained mixture model for growth and remodeling of soft tissues. *Mathematical Models and Methods in Applied Sciences* 12(03):407–430. <https://doi.org/10.1142/s0218202502001714>
- [18] Intengan HD, Schiffrin EL (2001) Vascular Remodeling in Hypertension. *Hypertension* 38(3):581–587. <https://doi.org/10.1161/hy09t1.096249>

- [19] Krommer AR, Ueberhuber CW (1998) Computational Integration pp 113–154. <https://doi.org/10.1137/1.9781611971460.ch5>
- [20] Latorre M, Humphrey JD (2018) A mechanobiologically equilibrated constrained mixture model for growth and remodeling of soft tissues. *ZAMM - Journal of Applied Mathematics and Mechanics / Zeitschrift für Angewandte Mathematik und Mechanik* 98(12):2048–2071. <https://doi.org/10.1002/zamm.201700302>
- [21] Latorre M, Humphrey JD (2018) Modeling mechano-driven and immuno-mediated aortic maladaptation in hypertension. *Biomechanics and Modeling in Mechanobiology* 17(5):1497–1511. <https://doi.org/10.1007/s10237-018-1041-8>
- [22] Latorre M, Humphrey JD (2020) Fast, rate-independent, finite element implementation of a 3D constrained mixture model of soft tissue growth and remodeling. *Computer Methods in Applied Mechanics and Engineering* 368:113156. <https://doi.org/10.1016/j.cma.2020.113156>
- [23] Maes L, Famaey N (2023) How to implement constrained mixture growth and remodeling algorithms for soft biological tissues. *Journal of the Mechanical Behavior of Biomedical Materials* 140:105733. <https://doi.org/10.1016/j.jmbbm.2023.105733>
- [24] Mousavi SJ, Avril S (2017) Patient-specific stress analyses in the ascending thoracic aorta using a finite-element implementation of the constrained mixture theory. *Biomechanics and modeling in mechanobiology* 16(5):1765–1777. <https://doi.org/10.1007/s10237-017-0918-2>
- [25] Mousavi SJ, Farzaneh S, Avril S (2019) Patient-specific predictions of aneurysm growth and remodeling in the ascending thoracic aorta using the homogenized constrained mixture model. *Biomechanics and Modeling in Mechanobiology* 18(6):1895–1913. <https://doi.org/10.1007/s10237-019-01184-8>, 1912.07884
- [26] Pfaller MR, Hörmann JM, Weigl M, et al. (2019) The importance of the pericardium for cardiac biomechanics: from physiology to computational modeling. *Biomechanics and Modeling in Mechanobiology* 18(2):503–529. <https://doi.org/10.1007/s10237-018-1098-4>, 1810.05451
- [27] Quarteroni A, Sacco R, Saleri F (2006) *Numerical Mathematics. Texts in Applied Mathematics* pp 379–422. https://doi.org/10.1007/978-3-540-49809-4_9
- [28] Rodriguez EK, Hoger A, McCulloch AD (1994) Stress-dependent finite growth in soft elastic tissues. *Journal of Biomechanics* 27(4):455–467. [https://doi.org/10.1016/0021-9290\(94\)90021-3](https://doi.org/10.1016/0021-9290(94)90021-3)
- [29] Rosen LA, Hollis TM, Sharma M (1974) Alterations in bovine endothelial histidine decarboxylase activity following exposure to shearing stresses. *Experimental and Molecular Pathology* 20(3):329–343. [https://doi.org/10.1016/0014-4800\(74\)90064-1](https://doi.org/10.1016/0014-4800(74)90064-1)
- [30] Sheidaei A, Hunley SC, Zeinali-Davarani S, et al. (2011) Simulation of abdominal aortic aneurysm growth with updating hemodynamic loads using a realistic geometry. *Medical Engineering & Physics* 33(1):80–88. <https://doi.org/10.1016/j.medengphy.2010.09.012>
- [31] The Trilinos Project Team (2024) The Trilinos Project Website. <https://trilinos.github.io>, accessed: 2024-01-25
- [32] Valentín A, Cardamone L, Baek S, et al. (2009) Complementary vasoactivity and matrix remodelling in arterial adaptations to altered flow and pressure. *Journal of The Royal Society Interface* 6(32):293–306. <https://doi.org/10.1098/rsif.2008.0254>
- [33] Valentín A, Humphrey JD, Holzapfel GA (2013) A finite element-based constrained mixture implementation for arterial growth, remodeling, and adaptation: Theory and numerical verification. *International Journal for Numerical Methods in Biomedical Engineering* 29(8):822–849. <https://doi.org/10.1002/cnm.2555>

- [34] Wilson JS, Baek S, Humphrey JD (2012) Importance of initial aortic properties on the evolving regional anisotropy, stiffness and wall thickness of human abdominal aortic aneurysms. *Journal of The Royal Society Interface* 9(74):2047–2058. <https://doi.org/10.1098/rsif.2012.0097>
- [35] Zeinali-Davarani S, Sheidaei A, Baek S (2011) A finite element model of stress-mediated vascular adaptation: application to abdominal aortic aneurysms. *Computer Methods in Biomechanics and Biomedical Engineering* 14(9):803–817. <https://doi.org/10.1080/10255842.2010.495344>